Science Advances
AAAS

Supplementary Materials for

Intracellular silicification by early-branching magnetotactic bacteria

Jinhua Li*, Peiyu Liu, Nicolas Menguy, Xingliang Zhang, Jian Wang, Karim Benzerara, Lianjun Feng, Lei Sun, Yue Zheng, Fanqi Meng, Lin Gu, Eric Leroy, Jialong Hao, Xuelei Chu, Yongxin Pan

*Corresponding author. Email: lijinhua@mail.iggcas.ac.cn

Published 13 May 2022, *Sci. Adv.* **8**, eabn6045 (2022)
DOI: 10.1126/sciadv.abn6045

The PDF file includes:

Other Supplementary Material for this manuscript includes the following:

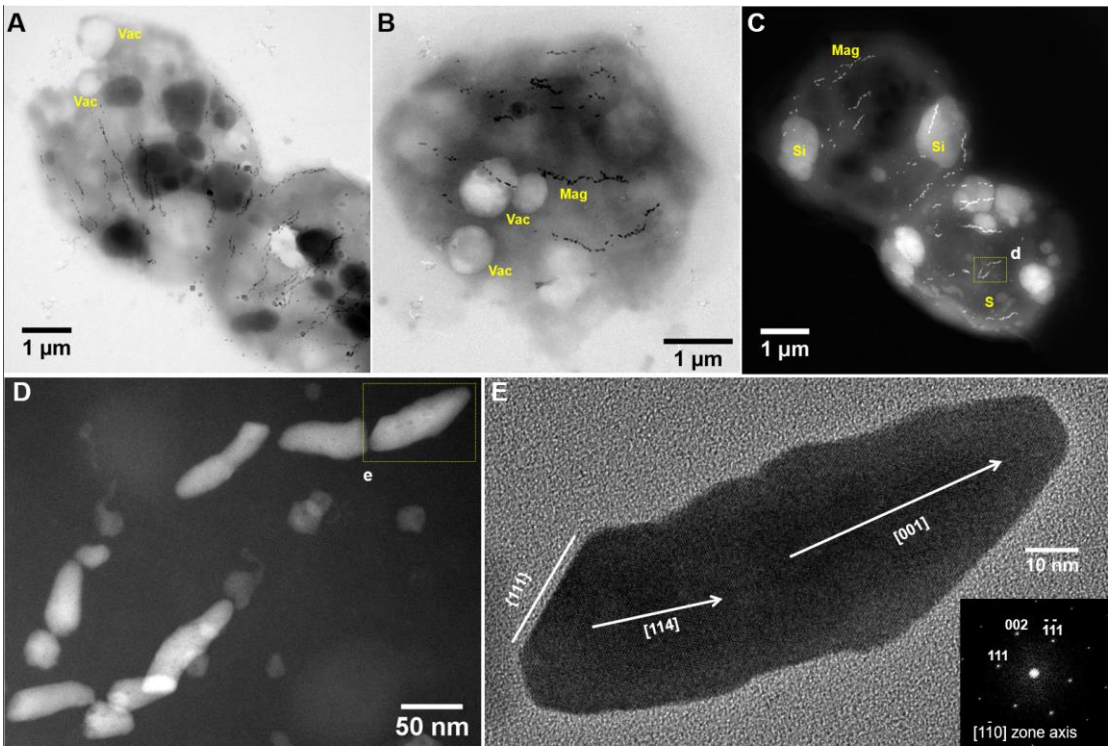

Fig. S1. Morphological features of WYHC-5. **(A-B),** Bright-field TEM images of three WYHC-5 cells showing intracellularly electron-transparent globules (i.e., vacuoles, Vac). **(C)**, HAADF-STEM image of two WYHC-5 cells showing three types of intracellularly electron-dense inclusions (Mag, magnetite magnetosomes; Si, silica granules; S, sulfur storage globules). **(D)**, Close-up of the bullet-shaped magnetic particles outlined by a yellow dashed square in (C). **(E)**, High resolution transmission electron microscopy (HRTEM) image of one single particle outlined by a yellow dashed square in (D). The inset is the corresponding indexed fast Fourier transform (FFT) pattern. The WYHC-5 cells are spherical-shaped and form vacuoles, magnetite-type magnetosomes, and other two types of intracellular inclusions (see Fig. S2 for details). Mature magnetosomes are curved bullet-shaped magnetite which are terminated by a big flat {111} face at the bottom end and small {100} face at the top end. The final elongation direction is uniformly along the [001] crystal direction. Such crystal morphology is similar to those of magnetosomes produced by *Candidatus* Magnetobacterium casensis strain MYR-1 (*79*).

.

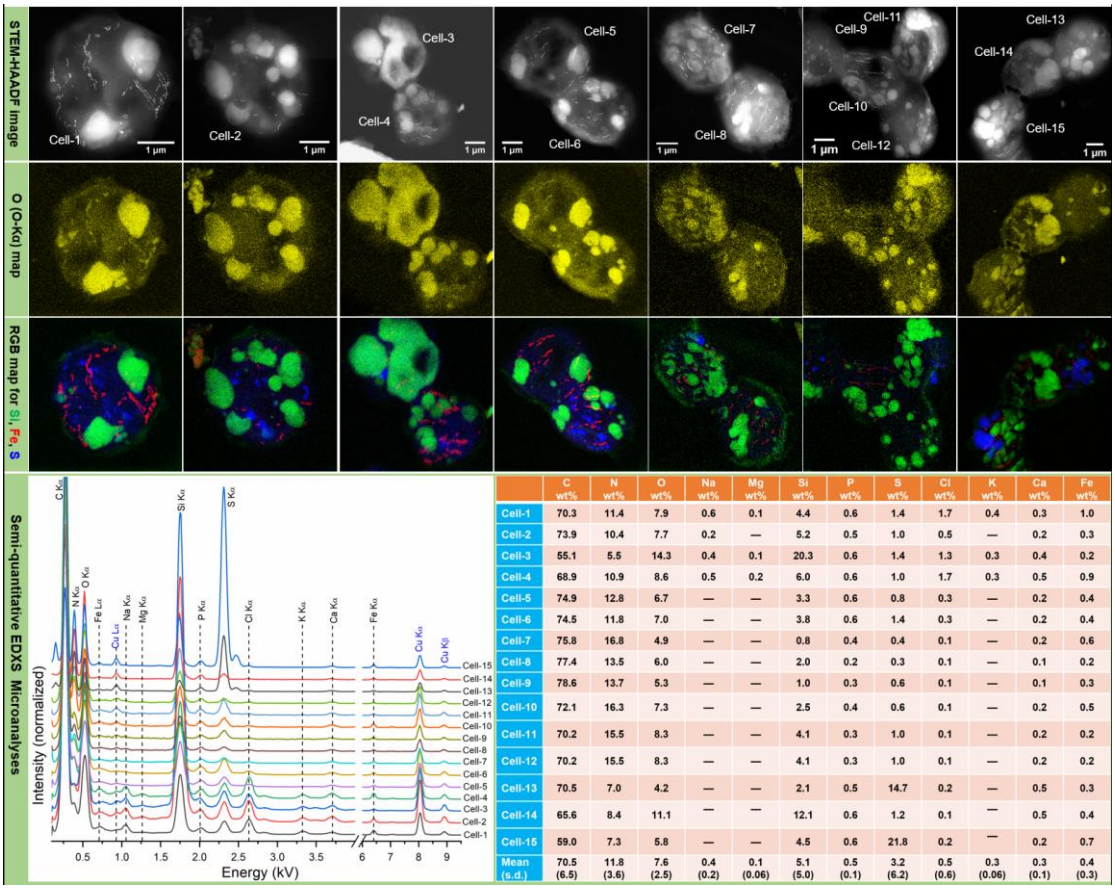

	C wt%	N wt%	O wt%	Na wt%	Mg wt%	Si wt%	P wt%	S wt%	Cl wt%	K wt%	Ca wt%	Fe wt%
Cell-1	70.3	11.4	7.9	0.6	0.1	4.4	0.6	1.4	1.7	0.4	0.3	1.0
Cell-2	73.9	10.4	7.7	0.2	—	5.2	0.5	1.0	0.5	—	0.2	0.3
Cell-3	55.1	5.5	14.3	0.4	0.1	20.3	0.6	1.4	1.3	0.3	0.4	0.2
Cell-4	68.9	10.9	8.6	0.5	0.2	6.0	0.6	1.0	1.7	0.3	0.5	0.9
Cell-5	74.9	12.8	6.7	—	—	3.3	0.6	0.8	0.3	—	0.2	0.4
Cell-6	74.5	11.8	7.0	—	—	3.8	0.6	1.4	0.3	—	0.2	0.4
Cell-7	75.8	16.8	4.9	—	—	0.8	0.4	0.4	0.1	—	0.2	0.6
Cell-8	77.4	13.5	6.0	—	—	2.0	0.2	0.3	0.1	—	0.1	0.2
Cell-9	78.6	13.7	5.3	—	—	1.0	0.3	0.6	0.1	—	0.1	0.3
Cell-10	72.1	16.3	7.3	—	—	2.5	0.4	0.6	0.1	—	0.2	0.5
Cell-11	70.2	15.5	8.3	—	—	4.1	0.3	1.0	0.1	—	0.2	0.2
Cell-12	70.2	15.5	8.3	—	—	4.1	0.3	1.0	0.1	—	0.2	0.2
Cell-13	70.5	7.0	4.2	—	—	2.1	0.5	14.7	0.2	—	0.5	0.3
Cell-14	65.6	8.4	11.1	—	—	12.1	0.6	1.2	0.1	—	0.5	0.4
Cell-15	59.0	7.3	5.8	—	—	4.5	0.6	21.8	0.2	—	0.2	0.7
Mean (s.d.)	70.5 (6.5)	11.8 (3.6)	7.6 (2.5)	0.4 (0.2)	0.1 (0.06)	5.1 (5.0)	0.5 (0.1)	3.2 (6.2)	0.5 (0.6)	0.3 (0.06)	0.3 (0.1)	0.4 (0.3)

Fig. S2. Chemical characterization of WYHC-5 cells at the nanoscale. Semi-quantitative chemical microanalyses of a total of 15 individual WYHC-5 cells based on 7 independent STEM-EDXS mapping measurements. The first row shows STEM-HAADF images of the cells; the second row shows their corresponding element maps of oxygen. The distribution of oxygen appears heterogeneous within the regions of cytoplasm, magnetosomes, and silica granules. The third row shows RGB maps of silicon (green), iron (red), and sulfur (blue), evidencing the spatial relationships of three types of intracellular inclusions. The bottom-left panel gathers the EDX spectra for all 15 WYHC-5 cells. Each EDX spectrum was obtained by manually extracting the signal from the cell region. The bottom-right table shows the semi-quantitative measurement of the mass concentration of each element within WYHC-5 cells. Notes: silica inclusions were observed within all these 15 cells, while sulfur globules were obviously founded within some of them with the exception for the cell-8, cell-10, and cell-14.

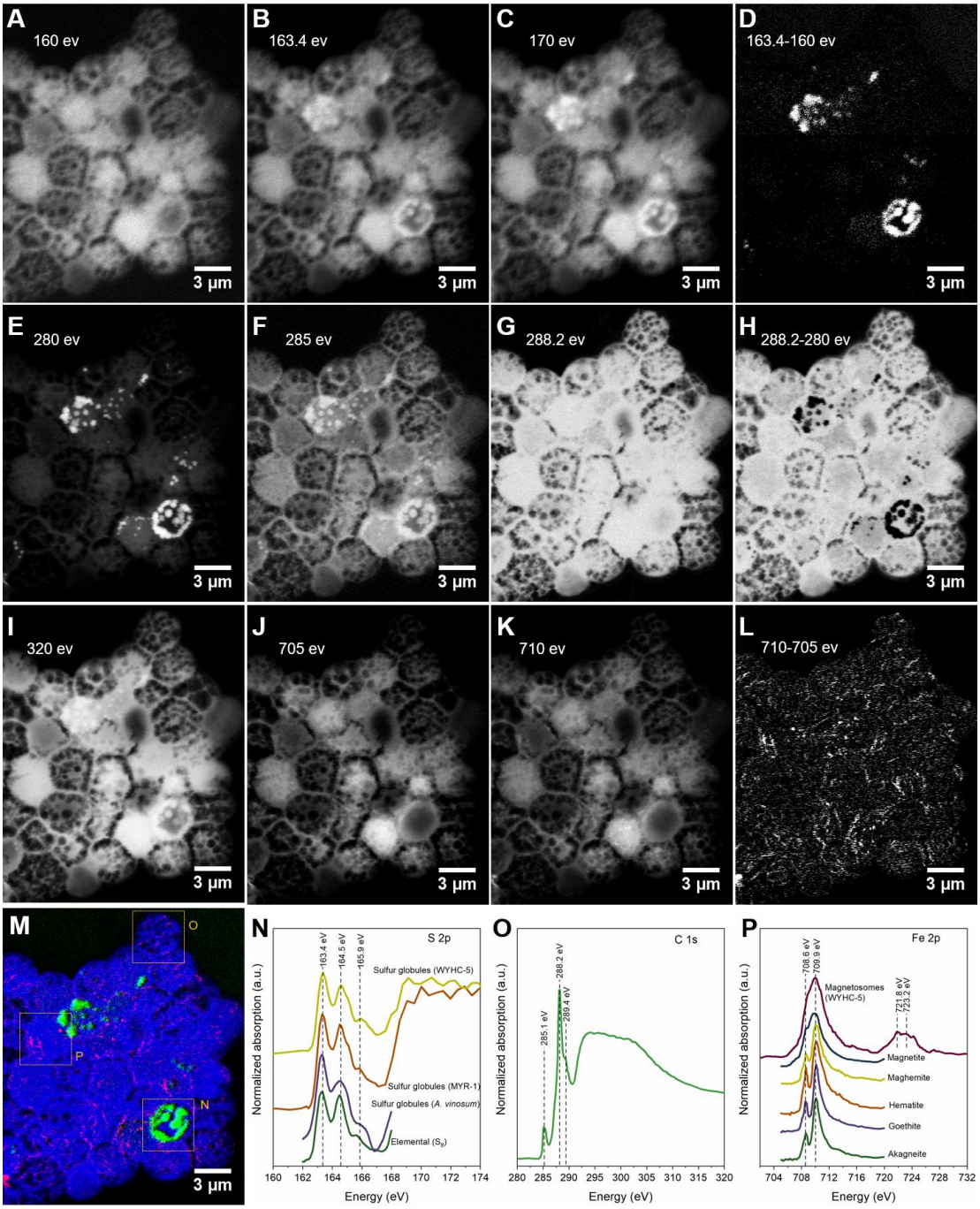

Fig. S3. Synchrotron radiation based STXM analyses of WYHC-5 cells. (A-L), STXM X-ray absorption images converted to optical density ($-\log(I/I_0)$) obtained at different energies: In the S $L_{2,3}$-edges region: **(A),** 160 eV; **(B)**, 163.4 eV; **(C)**, 170 eV. In the C K-edge region: **(E),** 280 eV; **(F)**, 285 eV; **(G)**, 288.2 eV; **(I)**, 320 eV. In the Fe $L_{2,3}$ region: **(J)**, 705 eV; **(K)**, 710 eV. The differences between two image pairs can be considered as sulfur, carbon, and iron maps. They are shown in **(D),** 163.4-160 eV; **(H),** 288.2-280 eV; **(L),** 710-705 eV, respectively. Vacuoles clearly appear in dark by STXM X-ray absorption imaging because they contain obviously less substance. (M) False color composite image of the same area as in (A-L), where the sulfur, carbon, and iron

signals are in green, blue, and red, respectively. Three individual WYHC-5 cells indicated by the dashed boxes were selected for acquiring a NEXAFS spectrum at the S $L_{2,3}$ edges (N), the C K-edge (O), and the Fe $L_{2,3}$ edge (P). The NEXAFS spectrum of S globules produced by WYHC-5 is compared with those of elemental sulfur (S_8) and sulfur globules produced by other bacteria (*21, 80, 81*). This demonstrates that the sulfur globules formed by WYHC-5 are composed of elemental sulfur (S^0) with a linear polymeric structure, identical to those formed by *Candidatus* Magnetobacterium casensis strain MYR-1 (*21*). The NEXAFS spectrum of WYHC-5 cell has a typical feature for bacterial cells with major peaks at 285.1 eV (aromatic groups) and 288.2 eV (amide carbonyl group/peptidic bond), and one small shoulder at 289.4 eV (carbonyl or alcohol groups) (*82*). The NEXAFS spectrum of Fe particles in WYHC-5 cells is compared with those of reference Fe oxi-(hydro)xides in Fe 2p (P) (*83*), consistent with TEM analyses, demonstrating WYHC-5 magnetosomes are magnetite. Notes: Chemical imaging analyses with synchrotron-based STXM on many cells (n = 39) showed that almost all WYHC-5 cells contain vacuoles and silica globules, and that only about 38.9% cells contain recognizable sulfur globules.

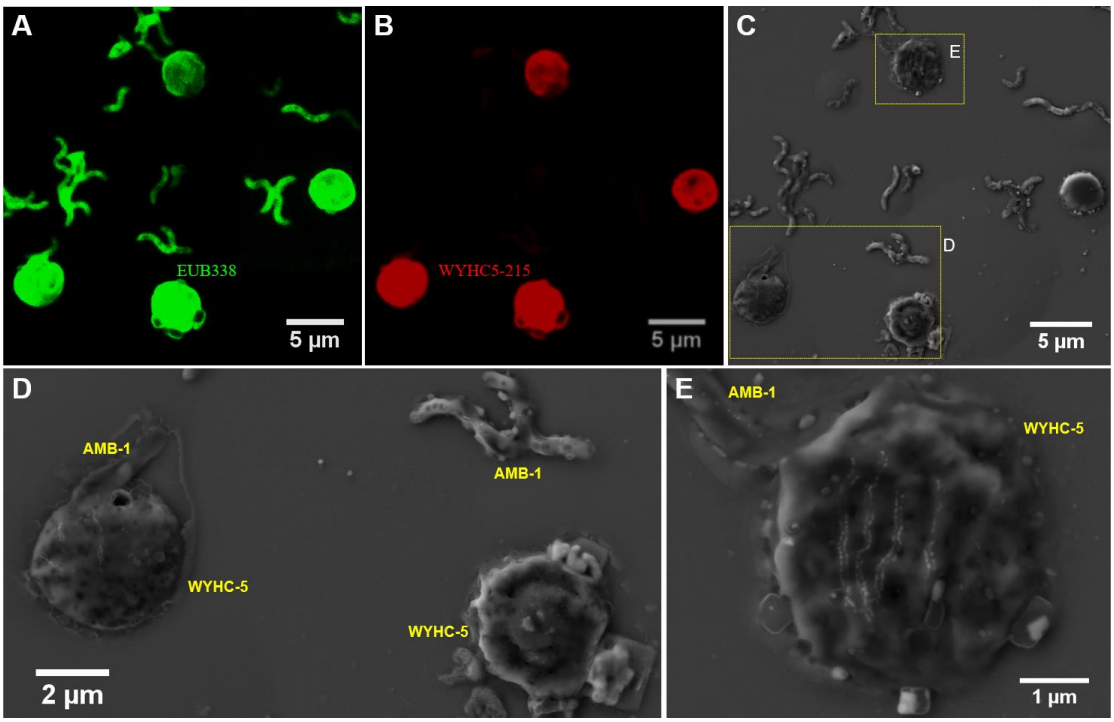

Fig. S4. Coupled FISH-SEM identification and phylogenetic analysis of WYHC-5 cells. (A-B), Epifluorescence microscope images of bacterial cells *in situ* hybridized with (A) the 5'-FAM-labelled universal bacterial probe EUB338, and (B) the 5'-Cy3-labelled WYHC-5-specific probe WYHC5-215. **(C)**, Low magnification SEM image of the same field view as in (A) and (B). **(D-E)**, High magnification SEM image of the boxed areas in (C) to show morphological features of WYHC-5 and inner controlled AMB-1 cells.

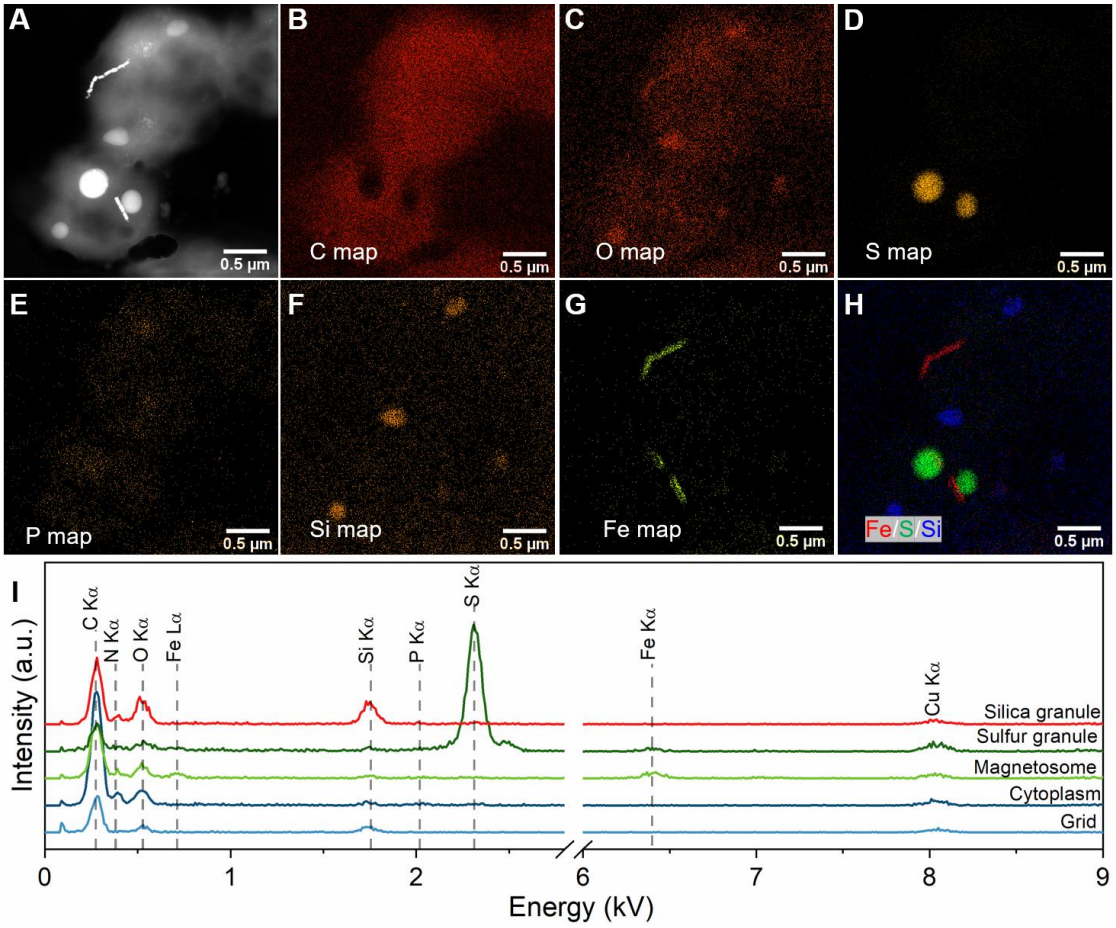

Fig. S5. STEM-EDXS elemental mapping (at HAADF mode) of alphaproteobacterial magnetotactic coccus strain YQC-1. (A), STEM-HAADF image of YQC-1 cell. **(B-G),** STEM-EDXS elemental maps of (B) C (C Kα), (C) O (O Kα), (D) S (S Kα), (E) P (P Kα), (F) Si (Si Kα), and (G) Fe (Fe Kα). **(H).** RGB map with Fe (red), S (green), and Si (blue). **(I),** EDXS spectra extracted from selected micro regions (100 nm diameter) of carbon film on the TEM grid, cytoplasm, magnetosome, sulfur granule, and silica globule.

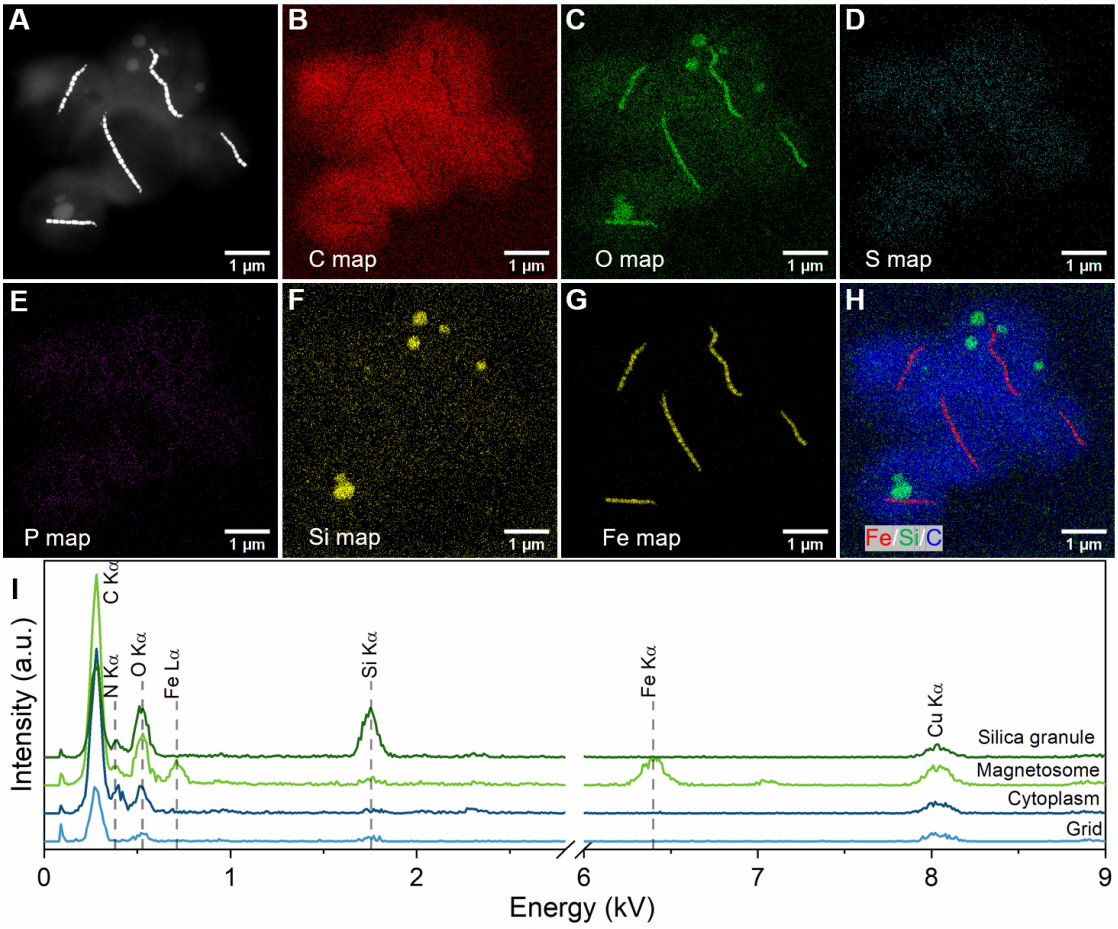

Fig. S6. STEM-EDXS elemental mapping (at HAADF mode) of alphaproteobacterial magnetotactic coccus strain WYHC-1. (A), STEM-HAADF image of WYHC-1 cell. **(B-G),** STEM-EDXS elemental maps of (B) C (C Kα), (C) O (O Kα), (D) S (S Kα), (E) P (P Kα), (F) Si (Si Kα), and (G) Fe (Fe Kα)**. (H),** RGB map with Fe (red), S (green), and Si (blue). **(I),** EDXS spectra extracted from selected micro regions (~100 nm diameter) of carbon film on the TEM grid, cytoplasm, magnetosome, sulfur granule, and silica globule.

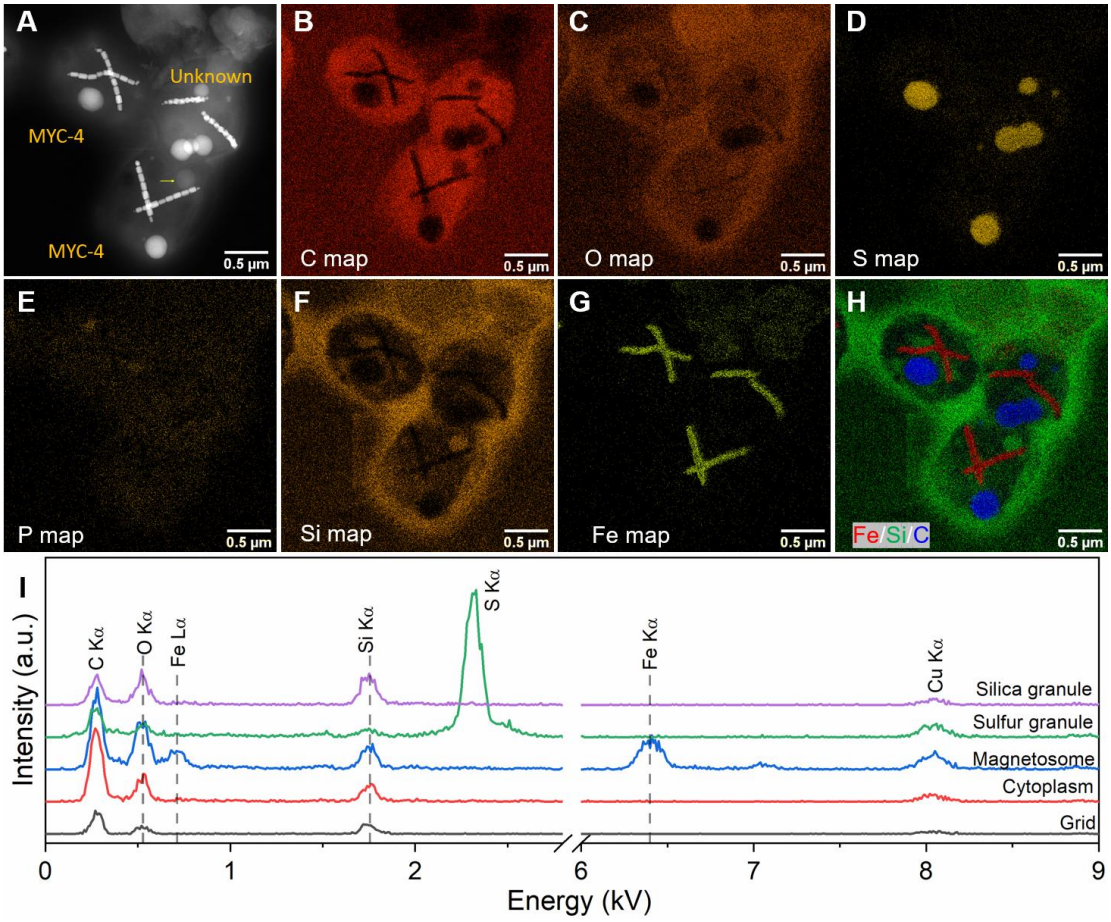

Fig. S7. STEM-EDXS elemental mapping (at HAADF mode) of alphaproteobacterial magnetotactic coccus strain MYC-4. (A), STEM-HAADF image of MYC-4 cell. **(B-G),** STEM-EDXS elemental maps of (B) C (C Kα), (C) O (O Kα), (D) S (S Kα), (E) P (P Kα), (F) Si (Si Kα), and (G) Fe (Fe Kα). **(H),** RGB map with Fe (red), S (green), and Si (blue). **(I),** EDXS spectra extracted from selected micro regions (~100 nm diameter) of carbon film on the TEM grid, cytoplasm, magnetosome, sulfur granule, and silica globule. The Si-rich globule is indicated by a yellow arrow in (A).

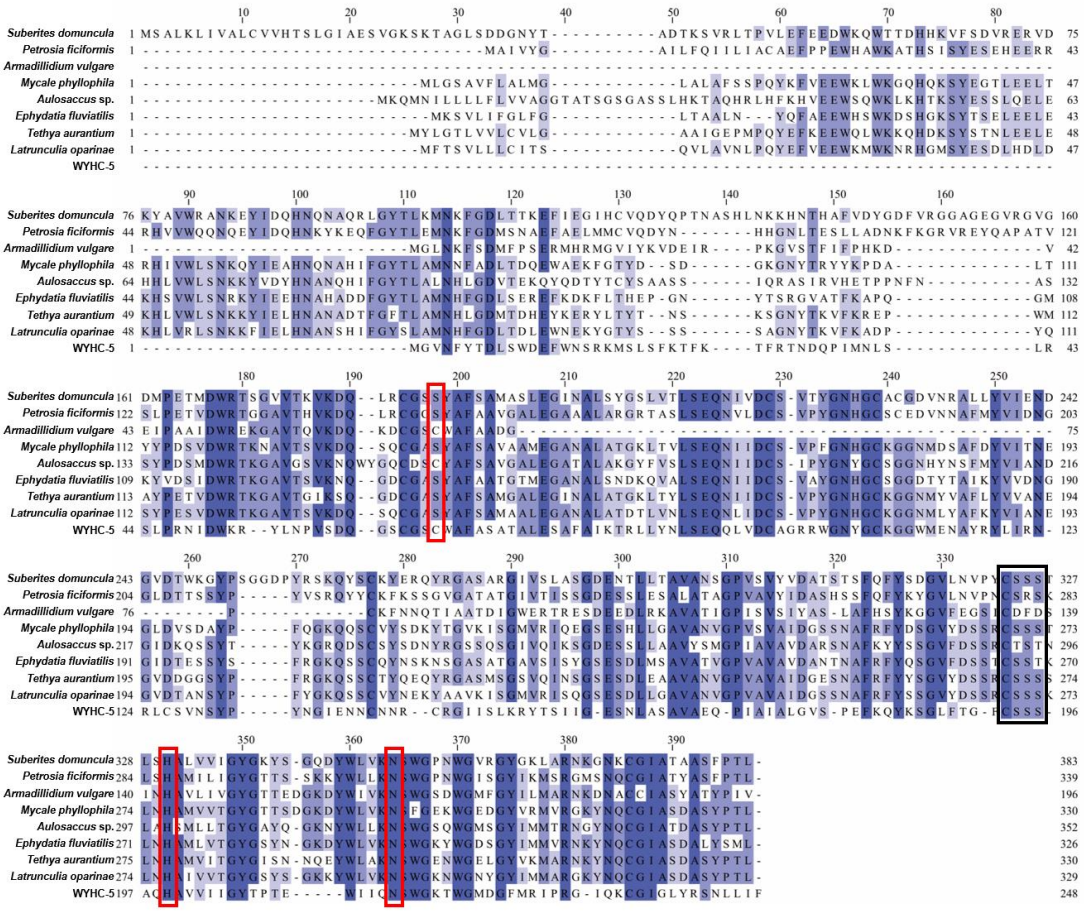

Fig. S8. Sequence alignment of silicatein from siliceous sponge species, *Armadillidium vulgare*, and strain WYHC-5. The amino acids forming the catalytic center (Ser or Cys, His, and Asn in all sequences) are highlighted by red boxes. The amino acids forming the serine cluster (Cys, Ser, Ser, and Ser in the silicatein from strain WYHC-5 and most siliceous sponge species) are highlighted by a black box. Residues conserved (similar or related with respect to their physico-chemical properties) in all sequences are shown in dark blue, and in at least two sequences are shown in white blue. Sequence IDs in NCBI Database are *Suberites domuncula* (CAI46304), *Petrosia ficiformis* (AAO23671), *Armadillidium vulgare* (RXG62397), *Mycale phyllophila* (AND80742), *Aulosaccus* sp. (ACU86976), *Ephydatia fluviatilis* (BAE54434), *Tethya aurantium* (AAF21819), *Latrunculia oparinae* (ACG63793), and strain WYHC-5 (OM416946).

Table S1. Size measurements of performed on WYHC-5 cells and inclusions

	Diameter of cell (μm)	Diameter of silica inclusion (μm)	Diameter of sulfur (S^0) inclusion (μm)	Diameter of vacuole (μm)	Diameter of carboxysome-like body (nm)	Magnetosome magnetite	
						Length (nm)	Width (nm)
No. of measurements	28 cells	113 inclusions	56 inclusions	30 particles	103 particles	503 particles	503 particles
Average	3.58	0.53	0.38	216.6	107.6	70.4	27.0
Standard deviation	0.42	0.34	0.23	64.7	14.8	27.5	6.3
Maximum value	4.57	2.69	0.98	369.5	149.7	160.4	36.8
Minimum value	2.73	0.08	0.09	200.2	105.5	12.1	9.8

Notes: The diameter of cell and the size of magnetosome magnetite were measured from bright-field TEM and STEM-HAADF images of air-dried cells. The diameters of silica and sulfur inclusions were measured from STEM-HAADF images of individual air-dried cells in which the silica and sulfur globules were chemically distinguished based on STEM-EDXS mapping analyses. The diameter of vacuole and carboxysome-like body were measured from TEM and STEM-HAADF images of ultrathin sections of freeze-substituted cells.

Table S2. 16S rRNA sequences retrieved from the sediments in laboratory microcosms collected from Lake Weiyanghu

Bacteria strain	No. of clones	Percentage of clones	Most similar strain	Accession	Identity
WYHC-5	28	93.3%	*Candidatus* Magnetoovum mohavensis strain LO-1	GU979422	98.3%
Leptothrix sp.	2	6.7%	*Leptothrix* sp. oral clone AW043	AF385534	99%

Table S3. MTB and their intracellular inclusions chemically identified by STEM-EDXS mapping analyses using HAADF mode

MTB Strain	Taxonomy	Environment	Intracellular inclusions	References
THC-1	‘*Ca.* Etaproteobacteria’	Freshwater	Polyphosphate granules; sulfur globules	(*84*)
SHHC-1		Brackish	Sulfur globules	(*85*)
MYC-4		Freshwater	Silica globules; sulfur globules	This study; (*30*)
WYHC-1		Freshwater	Silica globules	This study; (*30*)
YQC-1		Freshwater	Silica globules; sulfur globules	This study; (*30*)
AMB-1	Alphaproteobacteria	Freshwater	PHB granules	(*86*)
CCP-1		Freshwater	$CaCO_3$ granules	(*23*)
XQGS-1		Freshwater	$CaCO_3$ granules; calcium phosphate granules	(*24*)
WYHS-1		Freshwater	Polyphosphate granules; sulfur globules	(*20*)
SHHR-1	Gammaproteobacteria	Brackish	Polyphosphate granules; sulfur globules	(*32*)
GRS-1		Freshwater	Ca-bearing mineral granules	(*87*)
WYHR-1	Desulfobacterota	Freshwater	Polyphosphate granules	(*59*)
RS-1		Freshwater	Iron phosphate granules	(*88*)
MYR-1	Nitrospirota	Freshwater	Sulfur globules	(*79*)
WYHC-5		Freshwater	Silica globules; sulfur globules	This study
WGC		Marine	NA	(*89*)
BGC		Marine	Sulfur globules	(*89*)

Table S4. Concentration of water-soluble silica in the laboratory microcosms from several representative environments where MTB have been found

Ion species	LOD (ppm)	Freshwater				Marine	Salt pond
		WYH (ppm)	XQG (ppm)	MY (ppm)	YQ (ppm)	BLD (ppm)	FZS (ppm)
Water-soluble silica	0.1	31.8	24.4	41.5	43.6	18.4	10.5

Notes: The Limit of Detection (LOD) is the lowest concentration of a substance that can be reliably distinguished in this study. The Weiyanghu (WYH) and Xingqinggong (XQG) lakes are located at Xi'an city (Shaanxi Province) (*24, 59*), Miyun (MY) lake is located at Beijing city (*30*), Yuqiao (YQ) lake is located at Tianjin city (*30*), Bailudao (BLD) is located at the Bohai bay in Qinhuangdao city (Hebei Province) (*30*), Fuzhou saltern (FZS) is located at Bohai Bay in Dalian city (Liaoning Province) (*90*). The WYH, XQG, MY, and YQ lakes are freshwater environments, while the BLD bay and FZS salt pond are marine and hypersaline environments, respectively. Based on semi-quantitative calculation based on STEM-EDXS mapping analyses, WYHC-5 cells deposit silicon within their cells in the form of silica globules which occupy approximate 10.9% of the cell's total weight. This means that they can accumulate approximately ~3,500-fold higher than that in surrounding water during the experiments.

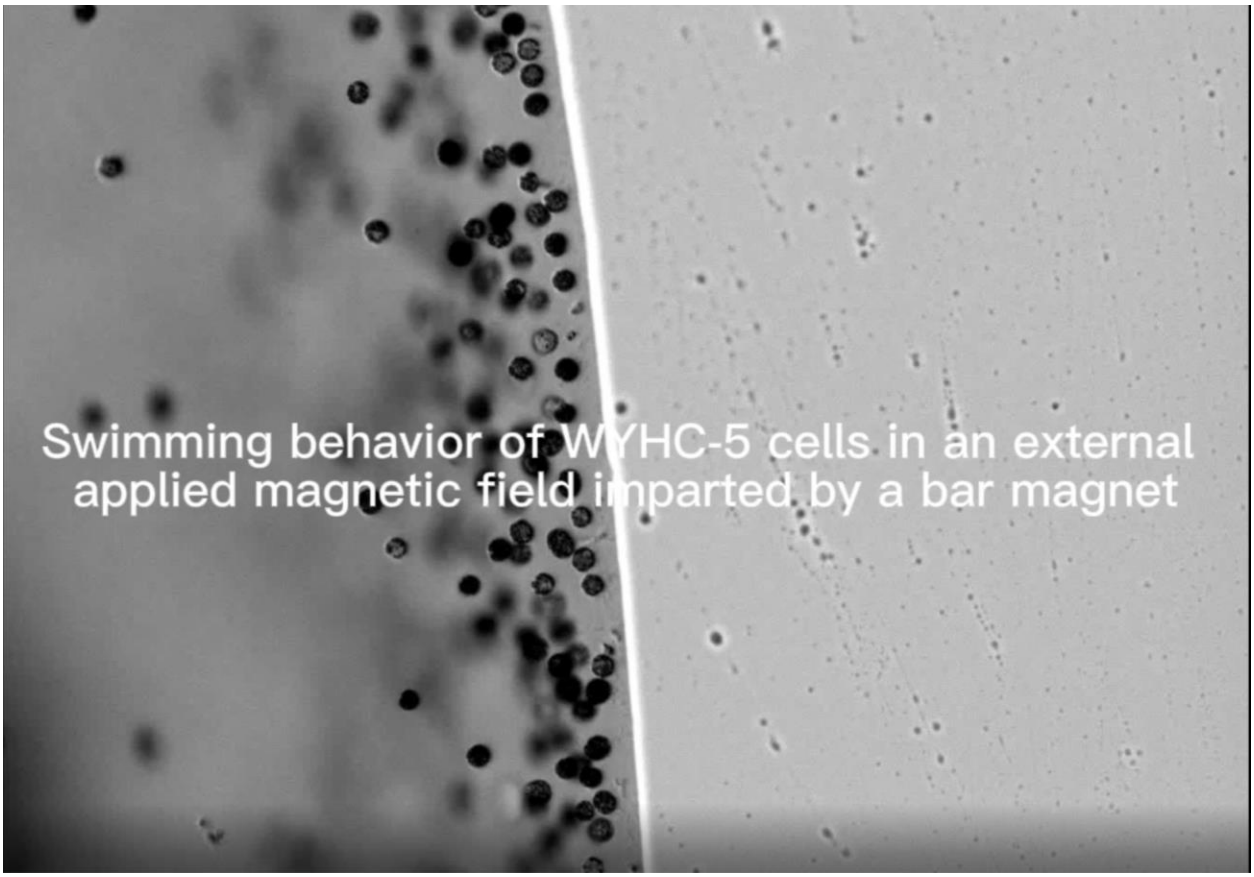

Movie S1. Swimming behavior of WYHC-5 cells in an external applied magnetic field imparted by a bar magnet.

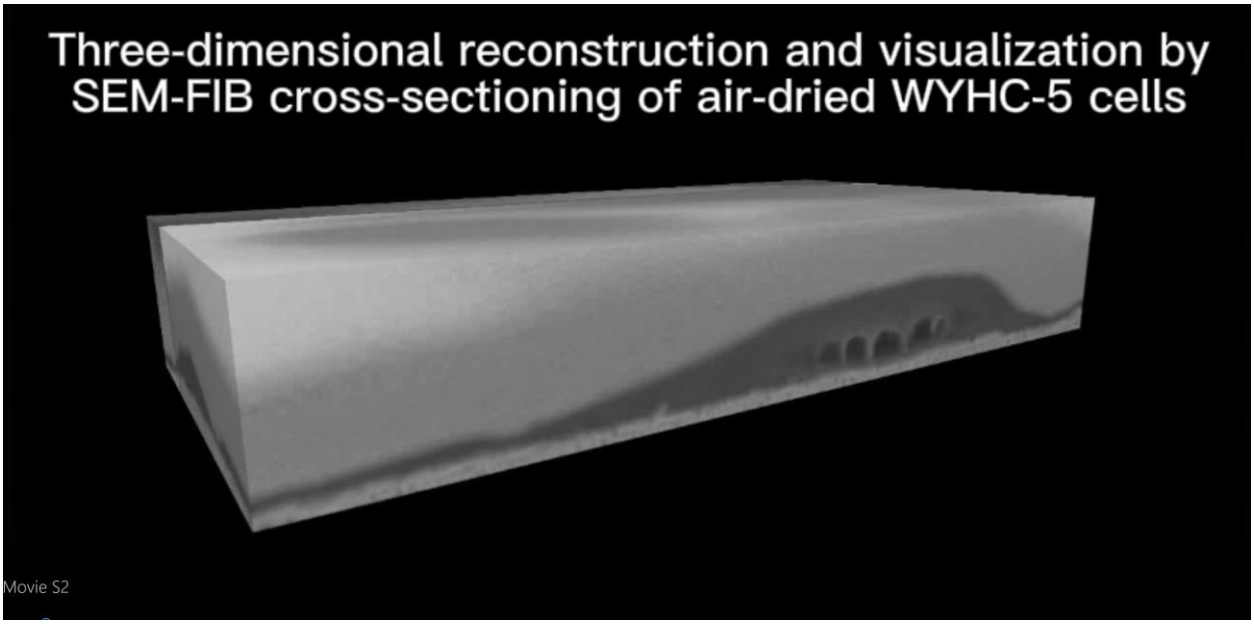

Movie S2. Three-dimensional reconstruction and visualization by SEM-FIB cross-sectioning of air-dried WYHC-5 cells.

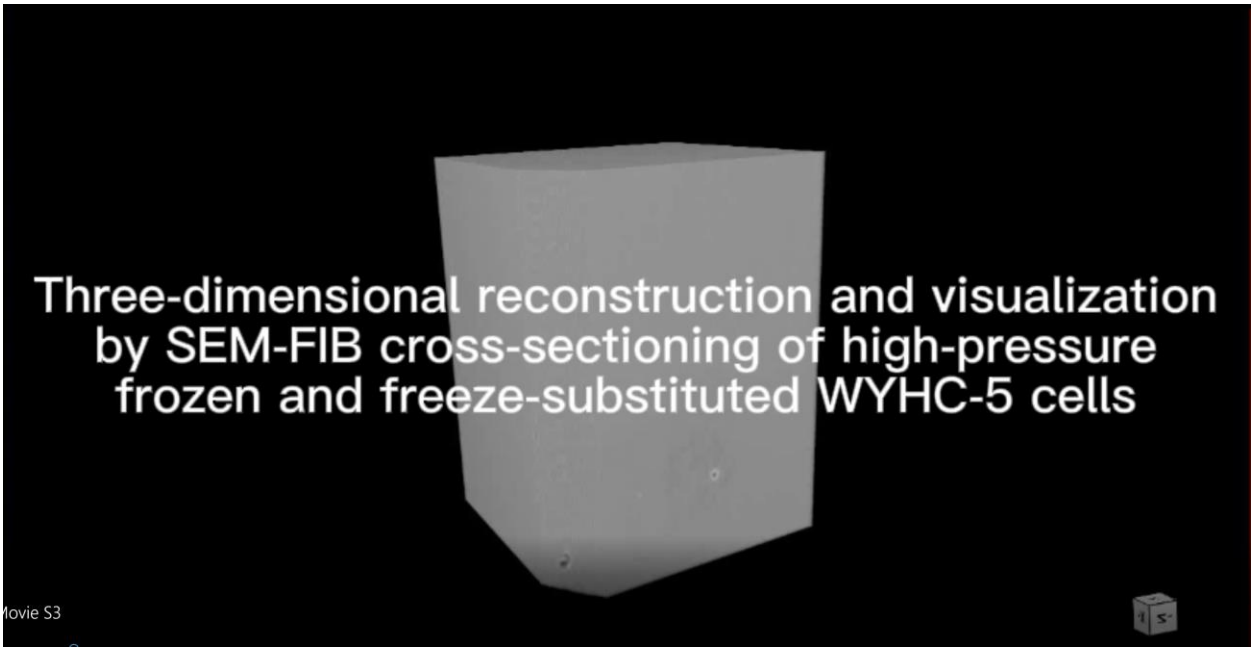

Movie S3. Three-dimensional reconstruction and visualization by SEM-FIB cross-sectioning of high-pressure frozen and freeze-substituted WYHC-5 cells

Data S1. List of sequences related to the formation of carboxysome and the fixation CO_2 via WL pathway

Data S2. List of sequences related to silica deposition and carbon metabolism in WYHC-5 genome.

Data S3. List of sequences related to silicon transporting within organisms

Data S4. List of sequences related to silica deposition within organisms

Data S5. Identification and distribution of silicon transporting and silica deposition within organisms

REFERENCES AND NOTES

1. F. De Tombeur, B. L. Turner, E. Laliberté, H. Lambers, G. Mahy, M.-P. Faucon, G. Zemunik, J.-T. Cornelis, Plants sustain the terrestrial silicon cycle during ecosystem retrogression. *Science* **369**, 1245–1248 (2020).

2. P. J. Tréguer, C. L. De La Rocha, The world ocean silica cycle. *Ann. Rev. Mar. Sci.* **5**, 477–501 (2013).

3. A. Marron, S. Ratcliffe, G. Wheeler, R. Goldstein, N. King, F. Not, C. de Vargas, D. Richter, The evolution of silicon transport in eukaryotes. *Mol. Biol. Evol.* **33**, 3226–3248 (2016).

4. A. H. Knoll, B. Kotrc, Protistan skeletons: A geologic history of evolution and constraint, in *Evolution of Lightweight Structures: Analyses and Technical Applications*, C. Hamm, Ed. (Springer, 2015), pp. 1–16.

5. R. G. Maliva, A. H. Knoll, B. M. Simonson, Secular change in the Precambrian silica cycle: Insights from chert petrology. *Geol. Soc. Am. Bull.* **117**, 835–845 (2005).

6. D. L. Kidder, D. H. Erwin, Secular distribution of biogenic silica through the Phanerozoic: Comparison of silica-replaced fossils and bedded cherts at the series level. *J. Geol.* **109**, 509–522 (2001).

7. R. Hirota, Y. Hata, T. Ikeda, T. Ishida, A. Kuroda, The silicon layer supports acid resistance of *Bacillus cereus* spores. *J. Bacteriol.* **192**, 111–116 (2010).

8. S. B. Baines, B. S. Twining, M. A. Brzezinski, J. W. Krause, S. Vogt, D. Assael, H. McDaniel, Significant silicon accumulation by marine picocyanobacteria. *Nat. Geosci.* **5**, 886–891 (2012).

9. T. Ikeda, Bacterial biosilicification: A new insight into the global silicon cycle. *Biosci. Biotechnol. Biochem.* **85**, 1324–1331 (2021).

10. K. Leblanc, V. Cornet, P. Rimmelin-Maury, O. Grosso, S. Hélias-Nunige, C. Brunet, H. Claustre, J. Ras, N. Leblond, B. Quéguiner, Silicon cycle in the tropical South Pacific: Contribution to the global

Si cycle and evidence for an active pico-sized siliceous plankton. *Biogeosciences* **15**, 5595–5620 (2018).

11. J. W. Krause, M. A. Brzezinski, S. B. Baines, J. L. Collier, B. S. Twining, D. C. Ohnemus, Picoplankton contribution to biogenic silica stocks and production rates in the Sargasso Sea. *Global Biogeochem. Cycles* **31**, 762–774 (2017).

12. K. R. Moore, M. Pajusalu, J. Gong, V. Sojo, T. Matreux, D. Braun, T. Bosak, Biologically mediated silicification of marine cyanobacteria and implications for the Proterozoic fossil record. *Geology* **48**, 862–866 (2020).

13. D. J. Conley, P. J. Frings, G. Fontorbe, W. Clymans, J. Stadmark, K. R. Hendry, A. O. Marron, C. L. De La Rocha, Biosilicification drives a decline of dissolved Si in the oceans through geologic time. *Front. Mar. Sci.* **4**, 397 (2017).

14. D. C. Ohnemus, J. W. Krause, M. A. Brzezinski, J. L. Collier, S. B. Baines, B. S. Twining, The chemical form of silicon in marine *Synechococcus*. *Mar. Chem.* **206**, 44–51 (2018).

15. M. A. Brzezinski, J. W. Krause, S. B. Baines, J. L. Collier, D. C. Ohnemus, B. S. Twining, Patterns and regulation of silicon accumulation in *Synechococcus* spp. *J. Phycol.* **53**, 746–761 (2017).

16. M. Schultze, Die Structur der Diatomeenschale verglichen mit gewissen aus Fluorkiesel künstlich darstellbaren Kieselhäuten, in *Verhandlungen des naturhistorischen Vereines der preussischen Rheinlande und Westphalens*, W. Co, Ed. (Cohen, 1863), pp. 1–41.

17. W. Lin, G. A. Patersona, Q. Zhu, Y. Wang, E. Kopylovad, Y. Li, R. Knight, D. A. Bazylinski, R. Zhu, J. L. Kirschvink, Y. Pan, Origin of microbial biomineralization and magnetotaxis during the Archean. *Proc. Natl. Acad. Sci. U.S.A.* **114**, 2171–2176 (2017).

18. C. T. Lefèvre, D. A. Bazylinski, Ecology, diversity, and evolution of magnetotactic bacteria. *Microbiol. Mol. Biol. Rev.* **77**, 497–526 (2013).

19. D. A. Bazylinski, R. B. Frankel, Magnetosome formation in prokaryotes. *Nat. Rev. Microbiol.* **2**, 217–230 (2004).

20. J. Li, P. Liu, A. Tamaxia, H. Zhang, Y. Liu, J. Wang, N. Menguy, X. Zhao, A. P. Roberts, Y. X. Pan, Diverse intracellular inclusion types within magnetotactic bacteria: Implications for biogeochemical cycling in aquatic environments. *J. Geophys. Res. Biogeosci.* **126**, e2021JG006310 (2021).

21. J. Li, P. Liu, J. Wang, A. P. Roberts, Y. Pan, Magnetotaxis as an adaptation to enable bacterial shuttling of microbial sulfur and sulfur cycling across aquatic oxic-anoxic interfaces. *J. Geophys. Res. Biogeosci.* **125**, e2020JG006012 (2020).

22. H. N. Schulz-Vogt, F. Pollehne, K. Jürgens, H. W. Arz, S. Beier, R. Bahlo, O. Dellwig, J. V. Henkel, D. P. R. Herlemann, S. Krüger, T. Leipe, T. Schott, Effect of large magnetotactic bacteria with polyphosphate inclusions on the phosphate profile of the suboxic zone in the Black Sea. *ISME J.* **13**, 1198–1208 (2019).

23. C. L. Monteil, K. Benzerara, N. Menguy, C. C. Bidaud, E. Michot-Achdjian, R. Bolzoni, F. P. Mathon, M. Coutaud, B. Alonso, C. Garau, D. Jézéquel, E. Viollier, N. Ginet, M. Floriani, S. Swaraj, M. Sachse, V. Busigny, E. Duprat, F. Guyot, C. T. Lefèvre, Intracellular amorphous Ca-carbonate and magnetite biomineralization by a magnetotactic bacterium affiliated to the *Alphaproteobacteria*. *ISME J.* **15**, 1–18 (2021).

24. P. Liu, Y. Liu, X. Ren, Z. Zhang, X. Zhao, P. Roberts Andrew, Y. Pan, J. Li, A novel magnetotactic *Alphaproteobacterium* producing intracellular magnetite and calcium-bearing minerals. *Appl. Environ. Microbiol.* **87**, e01556-21 (2021).

25. T. O. Yeates, C. A. Kerfeld, S. Heinhorst, G. C. Cannon, J. M. Shively, Protein-based organelles in bacteria: Carboxysomes and related microcompartments. *Nat. Rev. Microbiol.* **6**, 681–691 (2008).

26. C. A. Kerfeld, C. Aussignargues, J. Zarzycki, F. Cai, M. Sutter, Bacterial microcompartments. *Nat. Rev. Microbiol.* **16**, 277–290 (2018).

27. Y. G. Liao, *Practical Electron Microscopy and Database* (GlobalSino, 2013); www.globalsino.com/EM.

28. J. Wang, J. H. Li, Scanning transmission x-ray microscopy at the Canadian Light Source: Progress and selected applications in geosciences. *At. Spectrosc.* **43**, 84–98(2022).

29. V. K. Singh, A. L. Singh, R. Singh, A. Kumar, Iron oxidizing bacteria: Insights on diversity, mechanism of iron oxidation and role in management of metal pollution. *Environ. Sustain.* **1**, 221–231 (2018).

30. P. Liu, Y. Liu, X. Zhao, A. P. Roberts, H. Zhang, Y. Zheng, F. Wang, L. Wang, N. Menguy, Y. Pan, J. Li, Diverse phylogeny and morphology of magnetite biomineralized by magnetotactic cocci. *Environ. Microbiol.* **23**, 1115–1129 (2021).

31. C. T. Lefèvre, R. B. Frankel, F. Abreu, U. Lins, D. A. Bazylinski, Culture-independent characterization of a novel, uncultivated magnetotactic member of the *Nitrospirae* phylum. *Environ. Microbiol.* **13**, 538–549 (2011).

32. J. Li, H. Zhang, N. Menguy, K. Benzerara, F. Wang, X. Lin, Z. Chen, Y. Pan, Single-cell resolution of uncultured magnetotactic bacteria via fluorescence-coupled electron microscopy. *Appl. Environ. Microbiol.* **83**, e00409-17 (2017).

33. P. Yarza, P. Yilmaz, E. Pruesse, F. O. Glöckner, W. Ludwig, K.-H. Schleifer, W. B. Whitman, J. Euzéby, R. Amann, R. Rosselló-Móra, Uniting the classification of cultured and uncultured bacteria and archaea using 16S rRNA gene sequences. *Nat. Rev. Microbiol.* **12**, 635–645 (2014).

34. I. Gunnarsson, S. Arnórsson, Amorphous silica solubility and the thermodynamic properties of H_4SiO_4 in the range of 0° to 350°C at Psat. *Geochim. Cosmochim. Acta* **64**, 2295–2307 (2000).

35. W. E. G. Müller, A. Boreiko, X. Wang, S. I. Belikov, M. Wiens, V. A. Grebenjuk, U. Schloβmacher, H. C. Schröder, Silicateins, the major biosilica forming enzymes present in demosponges: Protein analysis and phylogenetic relationship. *Gene* **395**, 62–71 (2007).

36. K. Shimizu, D. E. Morse, "Silicatein: A unique silica-synthesizing catalytic triad hydrolase from marine sponge skeletons and its multiple applications," in *Methods in Enzymology*, B. S. Moore, Ed. (Academic Press, 2018), vol. 605, pp. 429–455.

37. K. Shimizu, J. Cha, G. D. Stucky, D. E. Morse, Silicatein α: Cathepsin L-like protein in sponge biosilica. *Proc. Natl. Acad. Sci. U.S.A.* **95**, 6234–6238 (1998).

38. H. C. Schröder, X. Wang, W. Tremel, H. Ushijima, W. E. G. Müller, Biofabrication of biosilica-glass by living organisms. *Nat. Prod. Res.* **25**, 455–474 (2008).

39. M. A. Chebbi, T. Becking, B. Moumen, I. Giraud, C. Gilbert, J. Peccoud, R. Cordaux, The genome of *Armadillidium vulgare* (Crustacea, Isopoda) provides insights into sex chromosome evolution in the context of cytoplasmic sex determination. *Mol. Biol. Evol.* **36**, 727–741 (2019).

40. K. Tamura, M. Nei, Estimation of the number of nucleotide substitutions in the control region of mitochondrial DNA in humans and chimpanzees. *Mol. Biol. Evol.* **10**, 512–526 (1993).

41. K. O. Konhauser, B. Jones, V. R. Phoenix, G. Ferris, R. W. Renaut, The microbial role in hot spring silicification. *Ambio* **33**, 552–558 (2004).

42. F. Orange, J.-R. Disnar, F. Westall, D. Prieur, P. Baillif, Metal cation binding by the hyperthermophilic microorganism, Archaea *Methanocaldococcus Jannaschii*, and its effects on silicification. *Palaeontology* **54**, 953–964 (2011).

43. K. Motomura, T. Ikeda, S. Matsuyama, M. A. Abdelhamid, T. Tanaka, T. Ishida, R. Hirota, A. Kuroda, The C-terminal zwitterionic sequence of CotB1 is essential for biosilicification of the *Bacillus cereus* spore coat. *J. Bacteriol.* **198**, 276–282 (2016).

44. V. Busigny, F. P. Mathon, D. Jézéquel, C. C. Bidaud, E. Viollier, G. Bardoux, J.-J. Bourrand, K. Benzerara, E. Duprat, N. Menguy, C. L. Monteil, C. T. Lefèvre, Mass collection of magnetotactic bacteria from the permanently stratified ferruginous Lake Pavin, France. *Environ. Microbiol.* **24**, 721–736 (2022).

45. F. Pfeifer, Distribution, formation and regulation of gas vesicles. *Nat. Rev. Microbiol.* **10**, 705–715 (2012).

46. C. Klaas, D. E. Archer, Association of sinking organic matter with various types of mineral ballast in the deep sea: Implications for the rain ratio. *Global Biogeochem. Cycles* **16**, 63-1–63-14 (2002).

47. W. Lin, A. Deng, Z. Wang, Y. Li, T. Wen, L.-F. Wu, M. Wu, Y. Pan, Genomic insights into the uncultured genus "*Candidatus* Magnetobacterium" in the phylum *Nitrospirae*. *ISME J.* **8**, 2463–2477 (2014).

48. T. J. Williams, C. L. Zhang, J. H. Scott, D. A. Bazylinski, Evidence for autotrophy via the reverse tricarboxylic acid cycle in the marine *magnetotactic coccus* strain MC-1. *Appl. Environ. Microbiol.* **72**, 1322–1329 (2006).

49. A. De Wever, K. Benzerara, M. Coutaud, G. Caumes, M. Poinsot, F. Skouri-Panet, T. Laurent, E. Duprat, M. Gugger, Evidence of high Ca uptake by cyanobacteria forming intracellular $CaCO_3$ and impact on their growth. *Geobiology* **17**, 676–690 (2019).

50. A. J. Milligan, F. M. M. Morel, A proton buffering role for silica in diatoms. *Science* **297**, 1848–1850 (2002).

51. S. Wenzl, R. Hett, P. Richthammer, M. Sumper, Silacidins: Highly acidic phosphopeptides from diatom shells assist in silica precipitation in vitro. *Angew. Chem. Int. Ed.* **47**, 1729–1732 (2008).

52. S. Arif, F. Liaquat, S. Yang, I. H. Shah, L. Zhao, X. Xiong, D. Garcia, Y. Zhang, Exogenous inoculation of endophytic bacterium *Bacillus cereus* suppresses clubroot (*Plasmodiophora brassicae*) occurrence in pak choi (*Brassica campestris* sp. chinensis L.). *Planta* **253**, 25 (2021).

53. K. R. Hendry, A. O. Marron, F. Vincent, D. J. Conley, M. Gehlen, F. M. Ibarbalz, B. Queguiner, C. Bowler, Competition between silicifiers and non-silicifiers in the past and present ocean and its evolutionary impacts. *Front. Mar. Sci.* **5**, 22 (2018).

54. C. C. Perry, Silicification: The processes by which organisms capture and mineralize silica. *Rev. Mineral. Geochem.* **54**, 291–327 (2003).

55. S. B. R. Chang, J. F. Stolz, J. L. Kirschvink, S. M. Awramik, Biogenic magnetite in stromatolites. II. Occurrence in ancient sedimentray environments. *Precambrian Res.* **43**, 305–315 (1989).

56. M. Amor, F. P. Mathon, C. L. Monteil, V. Busigny, C. T. Lefèvre, Iron-biomineralizing organelle in magnetotactic bacteria: Function, synthesis and preservation in ancient rock samples. *Environ. Microbiol.* **22**, 3611–3632 (2020).

57. H. Xu, Z. Shi, X. Zhang, M. Pang, K. Pan, H. Liu, Diatom frustules with different silica contents affect copepod grazing due to differences in the nanoscale mechanical properties. *Limnol. Oceanogr.* **66**, 3408–3420 (2021).

58. D. Schüler, The biomineralization of magnetosomes in *Magnetospirillum gryphiswaldense*. *Int. Microbiol.* **5**, 209–214 (2002).

59. J. Li, H. Zhang, P. Liu, N. Menguy, A. P. Roberts, H. Chen, Y. Wang, Y. Pan, Phylogenetic and structural identification of a novel magnetotactic *Deltaproteobacterium* strain WYHR-1 from a freshwater lake. *Appl. Environ. Microbiol.* **85**, e00731-19 (2019).

60. W. J. Zhang, L.-F. Wu, Flagella and swimming behavior of marine magnetotactic bacteria. *Biomolecules* **10**, 460 (2020).

61. M. Greenberg, K. Canter, I. Mahler, A. Tornheim, Observation of magnetoreceptive behavior in a multicellular magnetotactic prokaryote in higher than geomagnetic fields. *Biophys. J.* **88**, 1496–1499 (2005).

62. J. Li, I. M. Oliver, N. Cam, T. Boudier, M. Blondeau, E. Leroy, J. Cosmidis, F. Skouri-Panet, J.-M. Guigner, C. Férard, M. Poinsot, D. Moreira, P. Lopez-Garcia, C. Cassier-Chauvat, F. Chauvat, K. Benzerara, Biomineralization patterns of intracellular carbonatogenesis in cyanobacteria: Molecular hypotheses. *Minerals* **6**, 10 (2016).

63. M. Abad, F. Nieto, "Quantitative EDX analysis in TEM. Practical development, limitations and standards," in *Science, Technology and Education of Microscopy: An Overview*, A. Méndez-Vilas, Ed. (Formatex, 2003), pp. 687–694.

64. M. Blondeau, M. Sachse, C. Boulogne, C. Gillet, J.-M. Guigner, F. Skouri-Panet, M. Poinsot, C. Ferard, J. Miot, K. Benzerara, Amorphous calcium carbonate granules form within an intracellular compartment in calcifying cyanobacteria. *Front. Microbiol.* **9**, 1768 (2018).

65. C. Villinger, H. Gregorius, C. Kranz, K. Höhn, C. Münzberg, G. von Wichert, B. Mizaikoff, G. Wanner, P. Walther, FIB/SEM tomography with TEM-like resolution for 3D imaging of high-pressure frozen cells. *Histochem.Cell Biol.* **138**, 549–556 (2012).

66. C. Kizilyaprak, A. G. Bittermann, J. Daraspe, B. M. Humbel, FIB-SEM tomography in biology. *Methods Mol. Biol.* **1117**, 541–558 (2014).

67. A. Dereeper, V. Guignon, G. Blanc, S. Audic, S. Buffet, F. Chevenet, J.-F. Dufayard, S. Guindon, V. Lefort, M. Lescot, J.-M. Claverie, O. Gascuel, Phylogeny.fr: Robust phylogenetic analysis for the non-specialist. *Nucleic Acids Res.* **36**, W465–W469 (2008).

68. S. Kumar, G. Stecher, K. Tamura, MEGA7: Molecular evolutionary genetics analysis version 7.0 for bigger datasets. *Mol. Biol. Evol.* **33**, 1870–1874 (2016).

69. Y. J. Kim, N. Teletia, V. Ruotti, C. A. Maher, A. M. Chinnaiyan, R. Stewart, J. A. Thomson, J. M. Patel, ProbeMatch: Rapid alignment of oligonucleotides to genome allowing both gaps and mismatches. *Bioinformatics* **25**, 1424–1425 (2009).

70. A. M. Bolger, M. Lohse, B. Usadel, Trimmomatic: A flexible trimmer for Illumina sequence data. *Bioinformatics* **30**, 2114–2120 (2014).

71. Y. Peng, H. C. M. Leung, S. M. Yiu, F. Y. L. Chin, IDBA-UD: A *de novo* assembler for single-cell and metagenomic sequencing data with highly uneven depth. *Bioinformatics* **28**, 1420–1428 (2012).

72. G. V. Uritskiy, J. DiRuggiero, J. Taylor, MetaWRAP–A flexible pipeline for genome-resolved metagenomic data analysis. *Microbiome* **6**, 158 (2018).

73. D. H. Parks, M. Imelfort, C. T. Skennerton, P. Hugenholtz, G. W. Tyson, CheckM: Assessing the quality of microbial genomes recovered from isolates, single cells, and metagenomes. *Genome Res.* **25**, 1043–1055 (2015).

74. J. Besemer, A. Lomsadze, M. Borodovsky, GeneMarkS: A self-training method for prediction of gene starts in microbial genomes. Implications for finding sequence motifs in regulatory regions. *Nucleic Acids Res.* **29**, 2607–2618 (2001).

75. S. F. Altschul, T. L. Madden, A. A. Schäffer, J. Zhang, Z. Zhang, W. Miller, D. J. Lipman, Gapped BLAST and PSI-BLAST: A new generation of protein database search programs. *Nucleic Acids Res.* **25**, 3389–3402 (1997).

76. L.-T. Nguyen, H. A. Schmidt, A. Von Haeseler, B. Q. Minh, IQ-TREE: A fast and effective stochastic algorithm for estimating maximum-likelihood phylogenies. *Mol. Biol. Evol.* **32**, 268–274 (2015).

77. F. Sievers, D. G. Higgins, Clustal Omega for making accurate alignments of many protein sequences. *Protein Sci.* **27**, 135–145 (2018).

78. A. Waterhouse, M. Bertoni, S. Bienert, G. Studer, G. Tauriello, R. Gumienny, F. T. Heer, T. A. P. de Beer, C. Rempfer, L. Bordoli, R. Lepore, T. Schwede, SWISS-MODEL: Homology modelling of protein structures and complexes. *Nucleic Acids Res.* **46**, W296–W303 (2018).

79. J. Li, N. Menguy, C. Gatel, V. Boureau, E. Snoeck, G. Patriarche, E. Leroy, Y. Pan, Crystal growth of bullet-shaped magnetite in magnetotactic bacteria of the *Nitrospirae* phylum. *J. R. Soc. Interface* **12**, 20141288 (2015).

80. C. Karunakaran, A. Prange, J. Wang, Y. Lu, A. P. Hitchcock, J. Hormes, Speciation of sulphur globules in a single bacterial cell by sulphur 2p x-ray spectromicroscopy. *Canadian Light Source Res. Rep.*, 46–47 (2009).

81. C.-M. Teodorescu, D. Gravel, J. Choi, D. Pugmire, P. A. Dowben, N. Fominykh, A. A. Pavlychev, E. Rühl, Inner-shell excitation and fragmentation of sulfur aggregates. *J. Electron. Spectrosc. Relat. Phenom.* **101**, 193–198 (1999).

82. K. Benzerara, T. H. Yoon, T. Tyliszczak, B. Constantz, A. M. Spormann, G. E. Brown, Scanning transmission x-ray microscopy study of microbial calcification. *Geobiology* **2**, 249–259 (2004).

83. S.-Y. Chen, A. Gloter, A. Zobelli, L. Wang, C.-H. Chen, C. Colliex, Electron energy loss spectroscopy and *ab initio* investigation of iron oxide nanomaterials grown by a hydrothermal process. *Phys. Rev. B.* **79**, 104103 (2009).

84. J. Li, N. Menguy, E. Leroy, A. P. Roberts, P. Liu, Y. Pan, Biomineralization and magnetism of uncultured magnetotactic coccus strain THC-1 with non-chained magnetosomal magnetite nanoparticles. *J. Geophys. Res. Solid Earth* **125**, e2020JB020853 (2020).

85. H. Zhang, N. Menguy, F. Wang, K. Benzerara, E. Leroy, P. Liu, W. Liu, C. Wang, Y. Pan, Z. Chen, J. Li, Magnetotactic coccus strain SHHC-1 affiliated to *Alphaproteobacteria* forms octahedral magnetite magnetosomes. *Front. Microbiol.* **8**, 969 (2017).

86. J. Li, Y. Pan, G. Chen, Q. Liu, L. Tian, W. Lin, Magnetite magnetosome and fragmental chain formation of *Magnetospirillum magneticum* AMB-1: Transmission electron microscopy and magnetic observations. *Geophys. J. Int.* **177**, 33–42 (2009).

87. A. Taoka, J. Kondo, Z. Oestreicher, Y. Fukumori, Characterization of uncultured giant rod-shaped magnetotactic *Gammaproteobacteria* from a freshwater pond in Kanazawa, Japan. *Microbiology* **160**, 2226–2234 (2014).

88. M. E. Byrne, D. A. Ball, J. L. Guerquin-Kern, I. Rouiller, T. D. Wu, K. H. Downing, H. Vali, A. Komeili, *Desulfovibrio magneticus* RS-1 contains an iron- and phosphorus-rich organelle distinct from its bullet-shaped magnetosomes. *Proc. Natl. Acad. Sci. U.S.A.* **107**, 12263–12268 (2010).

89. X.-X. Qian, J. Liu, N. Menguy, J. Li, F. Alberto, Z. Teng, T. Xiao, W. Zhang, L.-F. Wu, Identification of novel species of marine magnetotactic bacteria affiliated with *Nitrospirae* phylum. *Environ. Microbiol. Rep.* **11**, 330–337 (2019).

90. P. Liu, A. Tamaxia, Y. Liu, H. Qiu, J. Pan, Z. Jin, X. Zhao, A. P. Roberts, Y. Pan, J. Li, Identification and characterization of magnetotactic *Gammaproteobacteria* from a salt evaporation pool, Bohai Bay, China. *Environ. Microbiol.* **24**, 938–950 (2022).